Clim Dyn (2015) 44:3111–3127
DOI 10.1007/s00382-014-2189-2

Energy-balance mechanisms underlying consistent large-scale temperature responses in warm and cold climates

Kenji Izumi · Patrick J. Bartlein · Sandy P. Harrison

Received: 2 February 2014 / Accepted: 18 May 2014 / Published online: 5 June 2014

Abstract Climate simulations show consistent large-scale temperature responses including amplified land–ocean contrast, high-latitude/low-latitude contrast, and changes in seasonality in response to year-round forcing, in both warm and cold climates, and these responses are proportional and nearly linear across multiple climate states. We examine the possibility that a small set of common mechanisms controls these large-scale responses using a simple energy-balance model to decompose the temperature changes shown in multiple *lgm* and *abrupt4* × CO_2 simulations from the CMIP5 archive. Changes in the individual components of the energy balance are broadly consistent across the models. Although several components are involved in the overall temperature responses, surface downward clear-sky longwave radiation is the most important component driving land–ocean contrast and high-latitude amplification in both warm and cold climates. Surface albedo also plays a significant role in promoting high-latitude amplification in both climates and in intensifying the land–ocean contrast in the warm climate case. The change in seasonality is a consequence of the changes in land–ocean and high-latitude/low-latitude contrasts rather than an independent temperature response. This is borne out by the fact that no single component stands out as being the major cause of the change in seasonality, and the relative importance of individual components is different in cold and warm climates.

Keywords Climate model simulations · Surface energy balance · Land–ocean contrast · Polar amplification · Seasonality change · Paleo/future simulations

1 Introduction

There are a number of common large-scale temperature responses to changes in forcing in simulations of past, historical, and future climates (Izumi et al. 2013), including (1) the differential responses of land and ocean to global warming or cooling, i.e. changes in the land–ocean contrast, (2) the tendency for temperature changes in the higher latitudes to be more extreme than changes in the tropics, i.e. high-latitude amplification, and (3) changes in seasonality in response to year-round changes in forcing. These responses are also shown in historical and paleoclimatic data. The consistency among simulated and observed temperature responses in the past (Izumi et al. 2013) implies that these are features of the climate system that are simulated successfully. The consistency of the simulated patterns of past and future temperature changes implies that a small set of common mechanisms controls the response of the climate system across multiple states. Previous studies have suggested that the consistency of the responses is inherent in the energetics and dynamics of the climate system (e.g. Dwyer et al. 2012; Fasullo 2010; Joshi

Electronic supplementary material The online version of this article (doi:10.1007/s00382-014-2189-2) contains supplementary material, which is available to authorized users.

K. Izumi (✉) · P. J. Bartlein
Department of Geography, University of Oregon, Eugene, OR 97403, USA
e-mail: izumi@uoregon.edu

S. P. Harrison
School of Biological Sciences, Macquarie University, North Ryde, NSW 2109, Australia

S. P. Harrison
Geography and Environmental Sciences, School of Human and Environmental Sciences, Reading University, Whiteknights, Reading, UK

et al. 2008; Screen and Simmonds 2010b). However, several different feedbacks are also potentially involved and the specific mechanisms are still matters of debate.

Here we review some of the previous studies that have focused on one or more of these large-scale responses in either warm or cold climates (or a few in both). We then attempt to diagnose the controls of these responses using an energy-balance approach to decompose the temperature changes shown in multiple simulations from the CMIP5 archive for both cold (*lgm*) and warm (*abrupt4* × CO_2) climates. We use a "bottom-up" approach that focuses first on map patterns of the components of temperature change, followed by an examination of zonal- and large-scale area-averages.

Land–ocean surface-temperature contrast, the generally larger amplitude of changes in land-surface temperature relative to those of the surrounding oceans, has been noted in both CO_2-induced warmer climate simulations (e.g. Sutton et al. 2007; Joshi et al. 2008) and CO_2-induced or decreased SST cooler climate simulations (e.g. Laine et al. 2009; Manabe et al. 1991; Joshi et al. 2008). The response is seen in both transient and equilibrium simulations, and thus the large heat capacity of ocean cannot be the primary reason for generation of the temperature contrast (Sutton et al. 2007). Several alternative mechanisms have been suggested to explain land–ocean contrast. First, Sutton et al. (2007), Laine et al. (2009) and Dong et al. (2009) suggested that the partitioning of the surface energy budget explains the contrast in the CO_2-induced warm or cold climates through changes in latent heat flux, cloud cover, or downward shortwave radiation. An increase in net downward radiation is compensated by an increase in latent heat flux over the oceans, but sensible heat flux increases over the land as the land dries out (Sutton et al. 2007). Drying of the land leads to reduction of cloud cover and increased downward shortwave radiation (Dong et al. 2009). Second, Joshi et al. (2008) and Byrne and O'Gorman (2013a) proposed that the difference between the moist- and dry-adiabatic lapse rates, and greater aridity over the land than ocean, leads to lower-tropospheric and surface-temperature increases over land when global temperatures increase; this hypothesis is based on the observation that temperature anomalies in the mid- and upper troposphere are zonally quite uniform because of efficient atmospheric transport, and is consistent with weak temperature-gradient hypothesis of Sobel and Bretherton (2000). Because the moisture source for the boundary layer over the land originates primarily from the oceans, an increase in boundary-layer moisture is constrained by the increase in specific humidity over the ocean, and by the Clausius–Clapeyron relation, and will thus fail to keep pace with saturation specific humidity over the land (Joshi et al. 2008). Land evaporation initially increases to compensate, but the land surface quickly begins to dry out, leading to further land warming. Third, Compo and Sardeshmukh (2009) showed that land warming is a response to ocean warming via "hydrodynamic-radiative teleconnections" such that moister and warmer air over the land results in increased longwave downward radiation at the surface.

Polar amplification is generally defined as trends (and variability) in near-surface air temperature that are larger in the Arctic/Antarctic regions than for the northern/southern hemisphere or globe as a whole (Serreze and Barry 2011; Taylor et al. 2013). This response is a near-universal feature of climate-model simulations under greenhouse gas-induced climate changes (e.g. Manabe and Stouffer 1980; Holland and Bitz 2003; Winton 2006), and is also seen in palaeoclimate simulations (e.g. Masson-Delmotte et al. 2006; Brady et al. 2013; Kageyama et al. 2013). Again, several different mechanisms have been proposed. Surface albedo feedback (*SAF*) has been shown to play a significant role in generating the amplification over the Arctic regions, where warming leads to a decrease in surface albedo through reduced ice and snow coverage, which in turn promotes further warming (and the reverse for cooling) (Hall 2004). Longwave (*LW*) radiation feedback from changes in cloud, water vapor, atmospheric CO_2 concentration, and air temperature has also been put forward as a mechanism to explain high-latitude amplification (see e.g. Lu and Cai 2009; Winton 2006; Graversen and Wang 2009; Pithan and Mauritsen 2014). Indeed, some model simulations without *SAF* have been shown to produce amplification through changes in *LW* radiation (Alexeev et al. 2005; Langen and Alexeev 2007; Lu and Cai 2010). Solomon (2006) showed that the increased availability of atmospheric moisture in a warmer climate will also cause enhanced warming of the Arctic regions through promoting stronger cyclones, leading to an increase in poleward heat transport (see also Graversen et al. 2008). Several authors (Holland et al. 2008; Deser et al. 2010; Jackson et al. 2010; Screen and Simmonds 2010b) have noted that a large part of the fall and winter temperature amplification is linked to sea-ice loss. Warming leads to thinner ice, which is subject to faster melt and increased heat flux through the ice, resulting in less continuous ice cover and a corresponding change of surface albedo and heat release from the ocean. Heat accumulated by the ocean as a result of the ice-albedo feedback mechanism is partially expended in making ice thinner, thus leading to an increase of surface temperatures in fall and winter. Serreze et al. (2009) and Screen and Simmonds (2010a) showed that the Arctic warming is strongest at the surface during most of the year and is primarily consistent with reductions in sea-ice cover. Finally, in some climate model analyses, a positive

wintertime feedback between convective clouds and sea-ice loss result in further warming and further sea-ice loss in CO_2-induced climate changes (Abbot et al. 2009; Leibowicz et al. 2012).

Seasonality, or the amplitude of the seasonal cycle of near-surface air temperature over the land has decreased in the last 50 years (e.g. Thomson 1995; Wallace and Osborn 2002; Stine et al. 2009; Stine and Huybers 2012). Climate models project a reduction in the amplitude of the seasonal cycle of near-surface air temperature over high-latitude regions due to late fall and early winter warming under greenhouse gas-induced warmer climates (e.g. Manabe and Stouffer 1980; Mann and Park 1996; Biasutti and Sobel 2009; Dwyer et al. 2012), and an increase in the amplitude of the seasonal cycle at the LGM (Izumi et al. 2013). Again several mechanisms have been put forward to explain these changes. First, sea-ice loss results in an increase of near-surface air temperature in late fall and winter over high-latitude regions due to an increase in heat release from the ocean (Manabe and Stouffer 1980; Manabe et al. 1991; Mann and Park 1996; Dwyer et al. 2012). Second, the changes over the tropics and mid-latitudes are controlled by changes in surface heat fluxes (Dwyer et al. 2012), and the easterly trade winds may influence the low-latitude changes in fluxes (Sobel and Camargo 2011). Third, Stine and Huybers (2012) show a strong relationship between interannual variations in the seasonal cycle and atmospheric circulation, in particular the winter circulation. Finally, it has been suggested that changes in shortwave optical properties can reduce the summertime maximum temperature due to a direct aerosol cooling effect (Wallace and Osborn 2002; Stine et al. 2009).

Thus previous studies have proposed number of different mechanisms for each large-scale temperature pattern in warm or cold climate, but not provided a comprehensive explanation for changes across both warm and climates or among the three large-scale responses. We exploit the fact that many of the models in the Coupled Modelling Intercomparison Project Phase 5 (CMIP5; Taylor et al. 2012) have made simulations of both past and future climates, to explore the key common controls of the large-scale temperature responses in both warmer and cooler climates. We first describe the data sources and processing (Sect. 2) and the energy-balance model we use to examine the generation of the large-scale responses (Sect. 3). We then decompose the large-scale responses using the energy-balance model and examine the global spatial patterns and zonal averages of surface temperature and its components (Sect. 4). We then summarize those large-scale patterns by describing large-scale area averages in warmer and cooler climates (Sect. 5). Finally, we discuss and summarize our findings (Sect. 6).

2 Data and analysis

We use global monthly mean surface temperature, surface radiative fluxes for both clear- and total-sky conditions, and surface latent- and sensible-heat fluxes from several Coupled Model Intercomparison Project Phase 5 (CMIP5) experiments, focusing on the *lgm,* and *abrupt4* $\times$ CO_2, experiments, expressed as anomalies relative to a pre-industrial control simulation (*piControl*). Details of the experimental design are given by (Taylor et al. 2012; Braconnot et al. 2012). The *lgm* experiment is an equilibrium simulation of the Last Glacial Maximum (LGM, ca 21,000 years ago) and was designed to examine the climate response to the presence of large ice sheets and lower greenhouse gas (GHG) concentration. The *abrupt4* $\times$ CO_2 experiment was designed to examine the response to an instantaneous quadrupling of atmospheric CO_2 concentration (relative to *piControl*, i.e. 1,120 ppm). Owing to the logarithmic relationship of global average temperature to CO_2 levels, the two simulations are comparable in terms of the difference in CO_2 forcing relative to that for pre-industrial conditions.

We examined anomalies of each of the temperature and energy-balance variables from six models (Table 1). These are the six models that have all necessary data (surface temperature, surface and TOA radiative fluxes in both all-sky and clear-sky condition, surface non-radiative flux, sea ice fraction, land ice fraction, and land–ocean mask) for basic

Table 1 Models with *piControl*, *lgm*, and *abrupt4* $\times$ CO_2 simulations from the CMIP5 archive

Model name	Resolution (no. of gridcells: lat, lon)		
	atmosphere	Ocean	Sea ice
Community Climate System Model version 4 (CCSM4)	192, 288	320, 384	320, 384
GISS ModelIE version 2, Russell ocean model (GISS-E2-R)	90, 144	90, 144	90, 144
L'Institut Pierre-Simon Laplace Coupled Model version 5A low resolution (IPSL-CM5A-LR)	96, 96	149, 182	149, 182
Model for Interdisciplinary Research on Climate, Earth System Model (MICROC-ESM)	64, 128	192, 256	192, 256
MPI Earth System Model running in low resolution grid and paleo mode, (MPI-ESM-P)	96, 192	220, 256	220, 256
Meteorological Research Institute Coupled General Circulation Model version 3 (MRI-CGCM3)	160, 320	360, 368	360, 368

analyses. We used the last 100 years of *lgm* and *piControl* simulations and the last 60 years of the *abrupt* $\times$ CO_2 simulation. The sign, magnitude and spatial patterns of the anomalies are broadly consistent from model to model across multiple climate states (see Fig. S1). We therefore calculated the ensemble-mean anomalies of each variable across the six models (Table 1) because the ensemble mean results are generally closer to observations than individual model results under the current climate (Gleckler et al. 2008). IPSL-CM5A-LR has not archived latent heat for the *lgm* simulation, so we constructed the ensemble anomaly using latent-heat values from the other five models. For mapping and the calculation of ensemble averages, the output from each model was interpolated to a regular 2° latitude-by-longitude grid using bilinear interpolation.

In comparing land and ocean temperatures we defined the land as all grid points where land-area fraction (*sftlf*: variable names are those used in the CMIP5 NetCDF data sets) is more than 40 % or sea-ice-area fraction (*sic*) is more than 40 %. High-latitude amplification is defined as the ratio of surface temperature (*ts*) changes over the Northern Hemisphere extratropics (NHEXT, 30°N–85°N) to those over the Northern Hemisphere tropics (NHT, 0°–30°N) or over the Southern Hemisphere extratropics (SHEXT, 30°S–85°S) to those over the Southern Hemisphere tropics (SHT, 0°–30°S). Seasonality change is defined as the difference between summer (June–July–August, JJA, in the northern hemisphere and December–January–February, DJF, in the southern hemisphere) and winter (DJF in the northern hemisphere and JJA in the southern hemisphere) mean surface temperature. All averages were area-weighted (by the area of the 2° $\times$ 2° grid cells).

We compare the spatial patterns of surface temperature changes and their partial-temperature-change (PTC) components in the *lgm* and *abrupt4* $\times$ CO_2 experiments. We measure the similarity of any two map patterns (e.g. those of the multi-model mean surface-temperature changes or the PTC of each component in the energy balance model) using the weighted uncentered anomaly correlation (AC_U) which measures the similarity of two patterns without removal of the global mean, thereby assessing agreement in magnitude as well as pattern (Wilks 2011, p. 364). The AC_U correlation coefficient is bounded by ± 1.0; $+1.0$ indicates a perfect match in spatial pattern between reference and simulation, and -1.0 indicates a completely opposite spatial pattern between reference and simulation.

3 Methods: decomposition of temperature anomaly patterns using the surface energy balance

An energy balance model can be used to quantify the roles of specific forcings and feedbacks in the generation of temperature anomaly patterns (e.g. Winton 2006; Laine et al. 2009; Lu and Cai 2009). For equilibrium climate states represented by the CMIP5 simulations, outgoing longwave radiation approximately balances the incoming absorbed solar radiation (i.e. the TOA net radiation values are close to zero; SI Table 1). For an ideal surface, the radiation that is absorbed by the surface must be balanced by the total of the energy radiated back to atmosphere, gained or lost by latent and sensible heat, and the change in heat storage. Thus, the surface energy balance can be written as:

$$\begin{aligned}\left(1-\alpha_{surf}\right)SW\downarrow_{surf}^{all}+LW\downarrow_{surf}^{all}&=LW\\ \uparrow_{surf}^{all}+Q_H+Q_E+Q_G,\end{aligned}\tag{1}$$

where α_{surf} is the surface albedo, which is the ratio of all-sky upward to downward shortwave radiation flux at the surface (i.e.$SW\uparrow_{surf}^{all}/SW\downarrow_{surf}^{all}$), and $LW\downarrow_{surf}^{all}$ and $LW\uparrow_{surf}^{all}$ are the all-sky downward and upward longwave radiation fluxes at the surface, Q_H and Q_E are the (nonradiative) surface sensible and latent heat fluxes, and Q_G is the flow of heat into or out of storage for land and or ocean (for oceans, this term includes the release of transported heat). Q_G is estimated as the residual term in the surface energy balance Eq. (1). For the radiative fluxes, positive values are defined to represent energy moving towards the surface, leading to surface warming, while negative values represent energy moving away from the surface, leading to surface cooling (Oke 1987). For the non-radiative fluxes, positive values represent flux away from the surface, leading to cooling, and negative toward surface, leading to surface warming. This sign convention thus associates radiative and non-radiative fluxes that either warm (positive) or cool (negative) the surface (Oke 1987).

The longwave radiation emitted by the surface can be represented by the Stefan–Boltzmann law for black bodies $LW\uparrow_{surf}^{all}=\varepsilon_{surf}\sigma T_{surf}^4$ where ε_{surf} is the emissivity of the surface, σ is Stefan's constant (5.67×10^{-8} W m^{-2} K^{-4}), and T_{surf} is the surface temperature (K). In practice, ε_{surf} is close to, but not exactly equal to 1.0 in the models (Jin and Liang 2006), and so following (Oke 1987)

$$LW\uparrow_{surf}^{all}=\varepsilon_{surf}\sigma T_{surf}^4+\left(1-\varepsilon_{surf}\right)LW\downarrow_{surf}^{all}.\tag{2}$$

However, if we assume that the emissivity of the surface (ε_{surf}) is close to 1.0 at all wavelengths, then the outgoing longwave radiation can be approximately represented as $LW\uparrow_{surf}^{all}\approx\sigma T_{surf}^4$. The surface energy budget can then be written:

$$\sigma T_{surf}^4\approx\left(1-\alpha_{surf}\right)SW\downarrow_{surf}^{all}+LW\downarrow_{surf}^{all}-Q_H-Q_E-Q_G.\tag{3}$$

Anomalies (relative to control) for the surface upward longwave radiation can be expressed as

$\Delta LW\uparrow^{all}_{surf} \approx 4\sigma T^3_{surf}\Delta T_{surf}$, where Δ is an anomaly operator that represents the experiment minus the *piControl* difference. Then, (2) can be rewritten as:

$$4\sigma T^3_{surf}\Delta T_{surf} \approx \Delta\left[(1-\alpha_{surf})SW\downarrow^{all}_{surf}\right] + \Delta LW\downarrow^{all}_{surf} - \Delta Q_H - \Delta Q_E - \Delta Q_G. \quad (4)$$

Following Lu and Cai (2009), the two radiative flux terms on the right-hand side of Eq. (3) can be decomposed into five radiative components: the surface albedo effect, surface shortwave cloud forcing, surface longwave cloud forcing, the change in surface clear-sky shortwave radiation, and the surface clear-sky longwave downward radiation. In the CMIP5 models, the surface albedo (α_{surf}) is generally >0.6 for continental ice, snow and sea ice, <0.1 for open ocean, and about 0.2 for vegetated ground. These differences mean that ice- and snow-covered areas play a strong role in the surface albedo effect (*SAE*) that warms or cools the climate in proportion to the size of ice- and snow-covered areas. The *SAE* can be quantified as follows:

$$SAE = -\Delta\alpha_{surf}\left(\overline{SW}\downarrow^{all}_{surf} + \Delta SW\downarrow^{all}_{surf}\right). \quad (5)$$

where the overbar denotes the *piControl* condition. The albedo effect is only active in a direct sense when shortwave radiation is received at the surface and thus is not important over polar regions in winter.

Surface cloud radiative forcing (CRF_{surf}) is defined as the difference between all-sky and clear-sky radiation at the surface:

$$\Delta SWCRF_{surf} = \Delta SW\downarrow^{all}_{surf} - \Delta SW\downarrow^{clr}_{surf}, \text{ and} \quad (6)$$

$$\Delta LWCRF_{surf} = \Delta LW\downarrow^{all}_{surf} - \Delta LW\downarrow^{clr}_{surf}, \quad (7)$$

where *clr* represents clear-sky conditions. $LWCRF_{surf}$ is a function of cloud temperature, height, and emissivity, and $SWCRF_{surf}$ is a function of cloud transmittance, surface albedo, and the solar zenith angle (Shupe and Intrieri 2004). Since a part of the *SAE* is included in the change of $SWCRF_{surf}$ (Soden et al. 2004), the surface albedo (α_{surf}) can be removed from the term as follows:

$$\Delta SWCRF_{surf} = (1-\overline{\alpha}_{surf})\Delta\left(SW\downarrow^{all}_{surf} - SW\downarrow^{clr}_{surf}\right). \quad (8)$$

It follows that the α_{surf} is removed from the change in surface clear-sky shortwave radiation, and the surface clear-sky shortwave radiation can be quantified as

$$(1-\overline{\alpha}_{surf})\Delta SW\downarrow^{clr}_{surf}, \quad (9)$$

where the overbar denotes the *piControl* condition. This term represents the change in GHG (in particular atmospheric CO_2 and water vapor) effects on clear-sky shortwave radiation. As the concentration of atmospheric GHGs increases, they absorb more incoming solar radiation in the atmosphere, leading to surface cooling, and the reverse is true.The change in surface clear-sky longwave downward radiation, $\Delta LW\downarrow^{clr}_{surf}$, represents the sum of downward longwave radiation changes at the surface due to changes in atmospheric water vapor, the moist static energy transport by atmospheric motion, and CO_2 concentration. The increase in water vapor at lower-levels in the atmosphere in a warmer climate results in increased emission of longwave radiation to the surface (Santer et al. 2007), and the reverse is true in a cooler climate.

If we divide Eq. 4 by $4\sigma\overline{T}^3_{surf}$, we can write

$$\underset{[a]}{\Delta T_{surf}} \approx \underset{[b]}{\Sigma_{EBC}/4\sigma\overline{T}^3_{surf}}, \text{ where} \quad (10)$$

$$\Sigma_{EBC} = \underset{[c]}{(SAE} + \underset{[d]}{\Delta SWCRF_{surf}} + \underset{[e]}{\Delta LWCRF_{surf}} + \underset{[f]}{(1-\overline{\alpha}_{surf})\Delta SW\downarrow^{clr}_{surf}} + \underset{[g]}{\Delta LW\downarrow^{clr}_{surf}} - \underset{[h]}{\Delta Q_H} - \underset{[i]}{\Delta Q_E} - \underset{[j]}{\Delta Q_G}), \quad (11)$$

(and the characters in square brackets correspond to the labels in Figs. 1, 2, 3 and 4). Each these terms shows the partial temperature change (PCT) contribution due to individual components of the energy balance to the total temperature anomaly (Lu and Cai 2009), and the sum of these contributions [b] will be approximately equal to the total surface temperature change. The surface temperature difference between [a] and [b] results from the linearization of surface upward longwave radiation adopted in the equation $\Delta LW\uparrow^{all}_{surf} \approx 4\sigma T^3_{surf}\Delta T_{surf}$ (Lu and Cai 2009), and a possible cause of this difference is variations of surface emissivity. If all the CMIP5 models had adopted the simple constant $\varepsilon_{surf} = 1.0$ in all climate states, [b] would be equal to [a]. However, almost all of the models adopt broadband surface emissivity ε_{surf} values slightly <1.0 (Jin and Liang 2006), and ε_{surf} depends on the surface types. Thus, there are changes in emissivity between different climate simulations because of the specification of different surface type. As a result, there is a residual term:

$$\Sigma_{EBC}/4\sigma\overline{T}^3_{surf} - \Delta T_{surf} \quad (12)$$

which is labeled [k] in the figures.

4 Responses of the global surface flux change

Figures 1 and 2 show the ensemble-average annual surface temperature differences and partial temperature changes (PTC) of each component under the *abrupt4* × CO_2 and *lgm* simulations. Depending on latitude and surface type (i.e. vegetated area/barren/ocean/sea ice/land ice), several

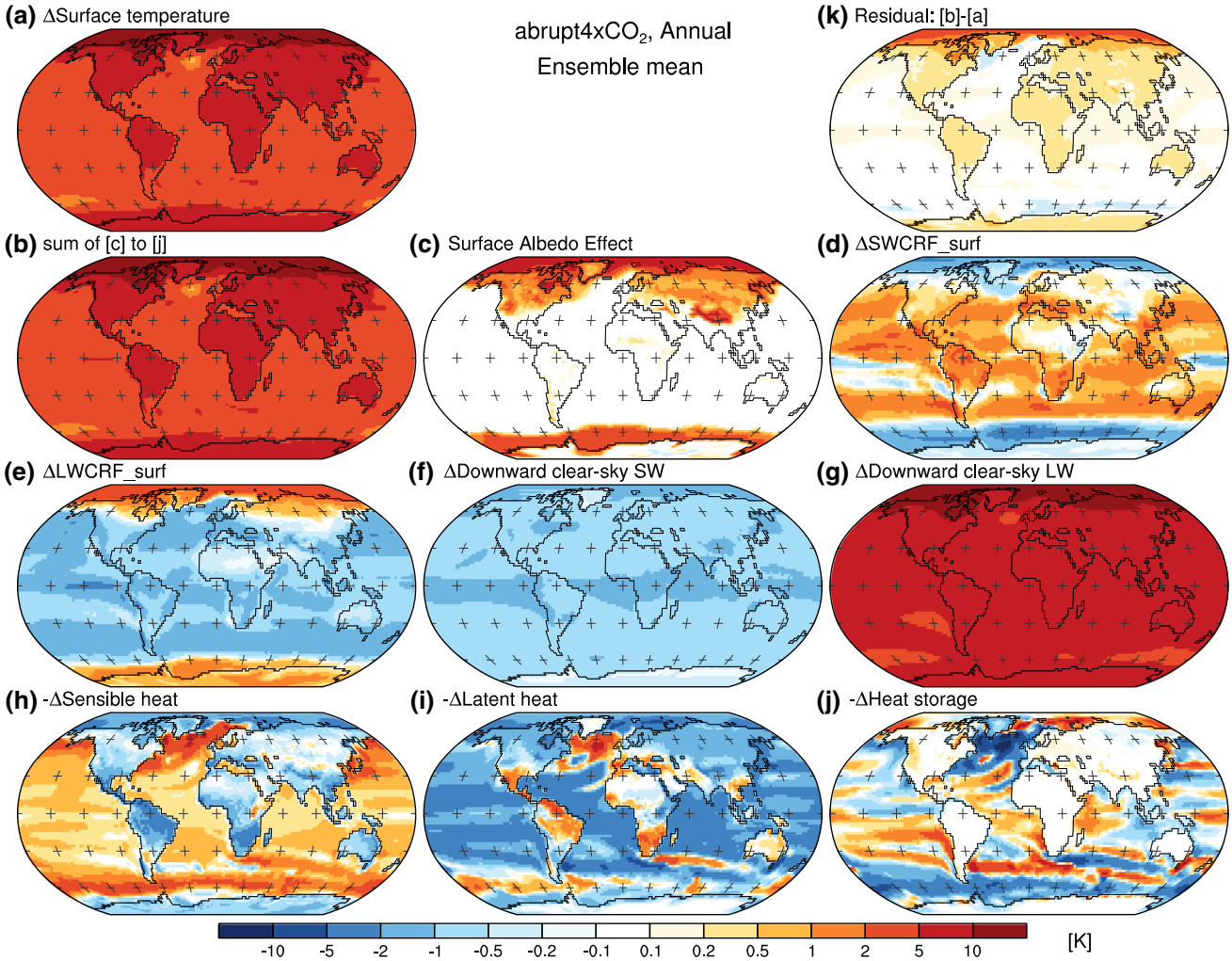

Fig. 1 Maps of ensemble-average annual temperature differences between the *abrupt4* × CO_2 and *piControl* simulations [a], and for the partial temperature change (PTC) of each component [b though j in Eq. 11], and the residuals [k] (Eq. 12)

components can be seen to be involved in the different responses. The responses of some components are robust, meaning that all models have the same responses (SI Figs. 2, 3). In order to elucidate the first-order pattern and amplitude for both surface temperature change and PTC of each component, we separately describe the global-average values and spatial correlations over the land, ocean and land and ocean all grids (Fig. 3). To summarize the map patterns and examine spatial variability that may be hidden in large-scale averages, we also show the zonal-mean annual surface temperature differences and PTC of components in both warm and cold climates (Fig. 4). (Other maps and zonal-mean figures for seasonal mean temperature changes appear in the in SI).

Annual-mean surface temperature for the *abrupt4* × CO_2 simulations increases over all grid points (4.94 K, relative to the *piControl* simulation, Figs. 1[a], 3[a], 4[a]). The differences are largest over land areas (6.82 K) and high-latitude ocean regions (Fig. 4[a]). The changes in winter (5.34 K for all grid points, 7.86 K for land, Fig. S4[a]) are larger than in summer (4.63 K for all grid points, 6.61 K for land, Fig. S5[a]). The models show similar responses over most regions (Fig. S2[a] and S10[a]–S15[a]) except that two models (CCSM4 and GISS-E2-R) show changes of the opposite sign over the Labrador Sea and northern North Atlantic Ocean. In contrast, annual-mean surface-temperature for the *lgm* simulation has a robust response (Figs. S3[a], S16[a]–21[a]) and decreases over all regions (−4.81 K, Figs. 2[a], 3[a], 4[a]), in particular over continental ice sheets, high latitude land, and sea-ice covered areas of the Arctic Ocean. Again, the amplitude of temperature change in winter (−5.28 K for all grid points, −9.38 K for land, Fig. S7[a]) is larger than in summer (−4.16 K for all grid points, −7.21 K for land, Fig. S8[a]).

The annual surface temperature changes estimated using the energy-balance model (term [b]) show almost the same

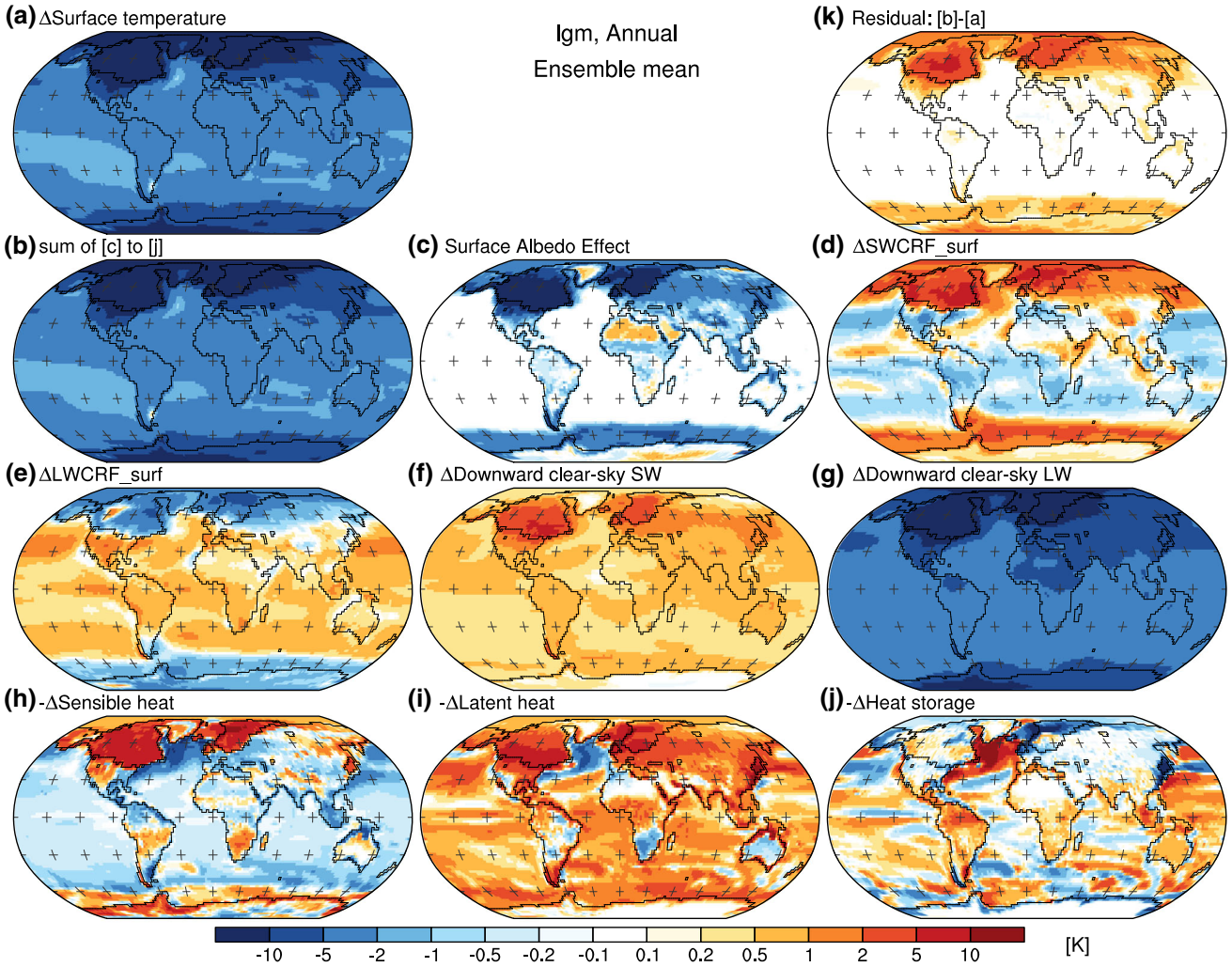

Fig. 2 Maps of ensemble-average annual temperature differences between the *lgm* and *piControl* simulations [a], and for the partial temperature change (PTC) of each component [b though j in Eq. 11], and the residuals [k] (Eq. 12)

amplitude (5.12 K for all grid points, Figs. 1[b], 3[b], 4[b]) and spatial pattern ($AC_U > 0.99$) in the *abrupt4* × CO_2 simulations as the amplitude of ΔT_{surf} calculated directly from the CMIP5 multi-model mean (i.e. [a]; 4.94 K). Thus, the energy-balance estimates of surface temperature changes adequately reproduce the simulated temperature changes. All models show similar patterns (Fig. S3[b]). Surface temperature is slightly higher over the land and over the Arctic Ocean compared to the temperatures calculated directly from the model output, and lower over the Labrador Sea and parts of the Southern Ocean (Fig. 1[b]). The average residual in the annual mean globally is 0.28 K over land areas, and 0.14 K over ocean areas. In contrast, the amplitude of the estimated surface-temperature changes in the *lgm* simulations are similar (−4.46 K for all grid points, Figs. 2[b], 3[b], 4[b]) to the values obtained directly from the CMIP5 model output (−4.81 K, Figs. 2[a], 3[a], 4[a]), and have very high AC_U values (>0.99). The energy-balance estimates are lower over land-ice or sea-ice covered areas (Fig. 2[b]); this results in a residual of annual-mean surface temperature over land of 0.8 K. In both cold and warm climates, the residuals result from surface emissivity (ε_{surf}) values that are not unity and from combinations of changes in ε_{surf}, surface temperature, and surface downward longwave radiation.

The PTC components show four basic spatial patterns (Figs. 1, 2, 3):

(1) broad-scale patterns that are uniform in sign with very high (positive/negative) spatial correlation, such as those for downward clear-sky longwave radiation ($\Delta LW\downarrow^{clr}_{surf}$ [g]) and downward clear-sky shortwave radiation ($(1-\overline{\alpha}_{surf})\Delta SW\downarrow^{clr}_{surf}$[f]);

(2) patterns that express surface-albedo contrasts with relatively high positive spatial correlation, such as (obviously) the surface albedo effect (SAE, [c]), but

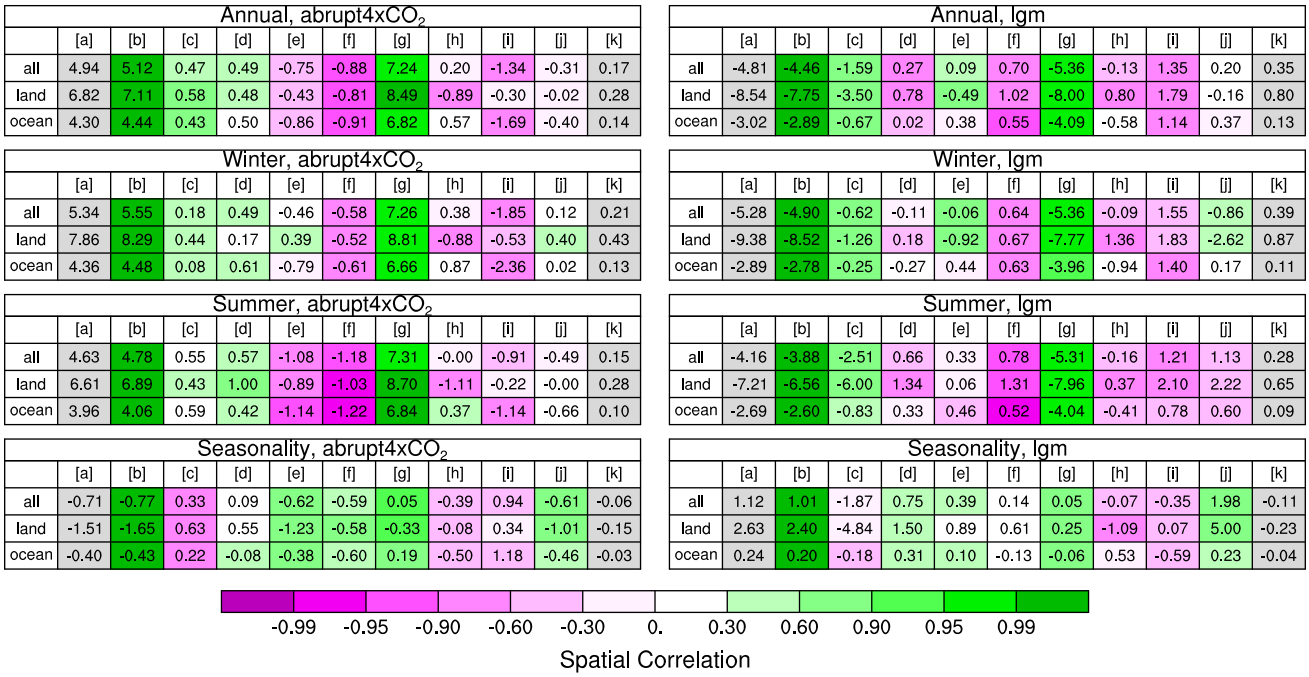

Fig. 3 Multimodel mean, area-weighted global (85°S–85°N) average surface temperature anomalies ([a] and [b], K) and partial temperature changes (PTC) of each component ([c]–[k], K) (*numbers*), and weighted uncentered anomaly correlations (*shading*) between the CMIP5 surface temperature differences [a] and the estimated surface temperature changes [b] and the PTC of each component ([c]–[j]) for the *abrupt4* × CO_2 simulations (*left*) and the *lgm* simulations (*right*). Summer means are for JJA in the Northern hemisphere and DJF in the southern hemisphere, winter means DJF in the northern hemisphere and JJA in the southern hemisphere, and seasonality means the difference between summer and winter

also surface shortwave cloud radiative forcing ($\Delta SWCRF_{surf}$ [d]) in the *lgm* simulations;

(3) patterns that show distinct land–ocean contrasts with relatively high negative spatial correlation, such as sensible heating ($-\Delta Q_H$ [h]) in the *abrupt4* × CO_2 simulations; and

(4) patterns that show distinct high-low latitude contrasts, such as surface longwave cloud radiative forcing ($\Delta LWCRF_{surf}$ [e]) in the *lgm* simulations.

Sea-ice and snow-covered areas decrease for the *abrupt4* × CO_2 simulation and increase for the *lgm* simulation. The surface albedo effect (*SAE*) contributes to the surface temperature increases over the polar and higher altitude areas in the *abrupt4* × CO_2 annual (Figs. 1[c], 4[c]) and summer (Figs. S5[c], S11[c]) climate. The *SAE* also reinforces the winter surface-temperature increases over the Northern Hemisphere mid-latitudes (Figs. S4[c], S10[c]). However, over most of the mid-latitudes and in the tropics the *SAE* is small and not robust. In the *lgm* simulations, SAE reinforces surface-temperature decreases over the Arctic and Antarctic Oceans and mid- and high latitude land areas (particularly over the continental ice sheets), for annual (Figs. 2[c], 4[c]) and summer mean climates (Figs. S8[c], S11[c]) and to the decreases in surface temperature over the middle-latitude land regions in winter (Figs. S7[c], S10[c]). The annual-mean PTC attributable to *SAE* over land is −3.50 and −6.0 K in summer with relatively high spatial correlation (Fig. 3[c]).

In the *abrupt4* × CO_2 experiments, surface shortwave cloud radiative forcing ($\Delta SWCRF_{surf}$, [d]) tends to reinforce surface temperature increases over the low- and middle-latitudes but to reduce positive temperature anomalies over the high latitudes regions (in particular the North Atlantic and the Arctic Oceans) annually (Figs. 1[d], 4[d]) and during the summer (Figs. S5[d], S11[d]). In the *lgm* simulations, in contrast, $\Delta SWCRF_{surf}$ reinforces the negative surface temperature anomalies in low latitudes and reduces the negative anomalies in high latitudes (Figs. 2[d], 4[d]), and has an effect opposite to SAE over high latitude regions. The large-scale spatial patterns are similar in both winter and summer (Figs. S7[d], S8[d]), but the amplitude of PTC (in particular, on the continental ice-sheets) is much larger in summer (Fig. S11[d]) than in winter (Fig. S10[d]).

In the *abrupt4* × CO_2 experiments, surface longwave cloud radiative forcing ($\Delta LWCRF_{surf}$[e]) reinforces increases in surface temperature over high latitude regions (in particular, the Arctic Ocean) but acts to reduce the temperature increase over the low and middle latitude regions in annually (Figs. 1[e], 4[e]) and winter

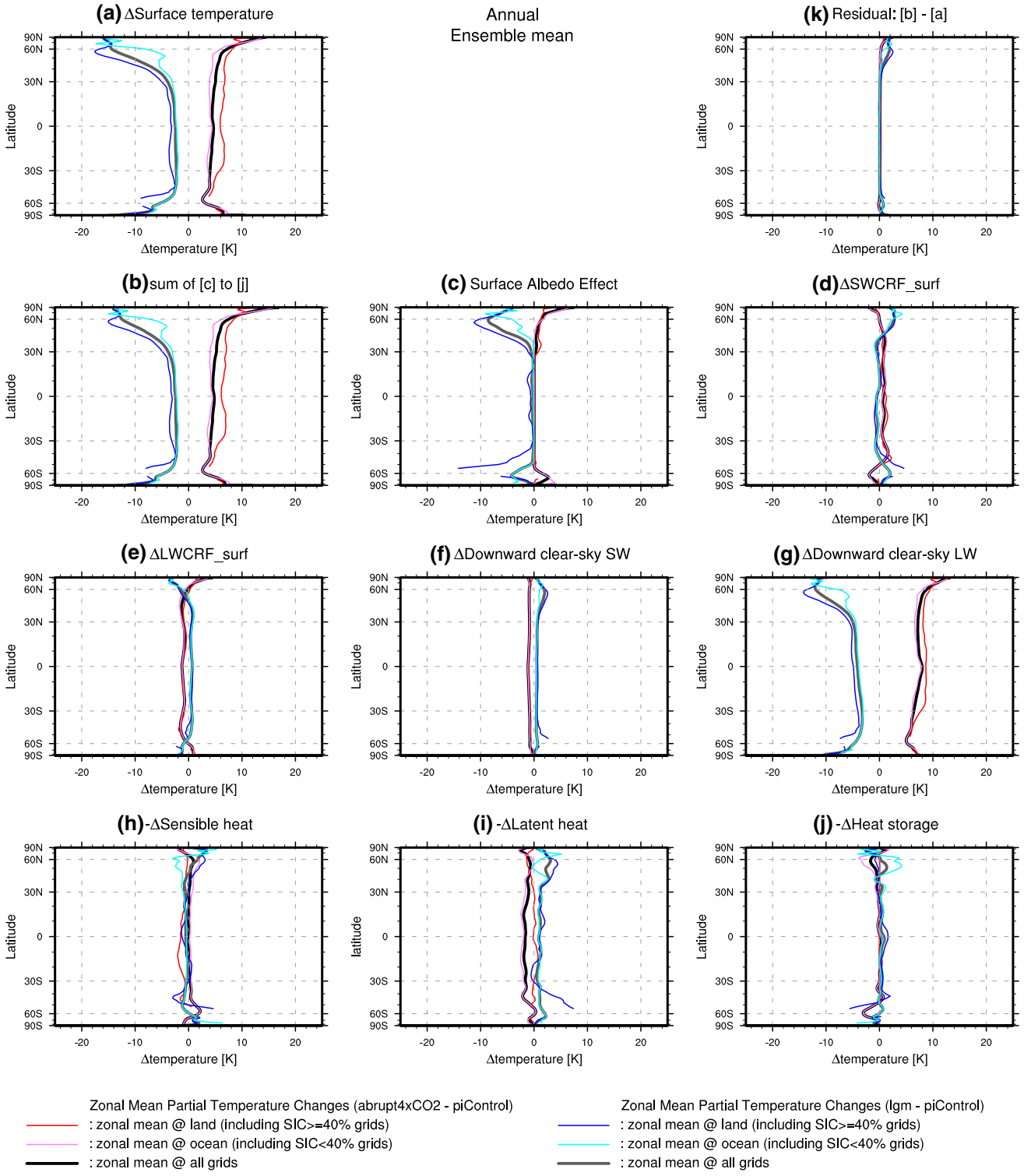

Fig. 4 The ensemble-average zonal-mean annual surface temperature differences between the *abrupt4* × CO_2 and *lgm* and *piControl* simulations [a], and for the partial temperature change (PTC) of each component [b though j in Eq. 11], and the residuals [k] (Eq. 12); *bold black* (land + ocean), *red* (land only), and *pink* (ocean only) for *abrupt4* × CO_2; *bold gray* (land + ocean), *blue* (land only), and *light blue* (ocean only) for *lgm*

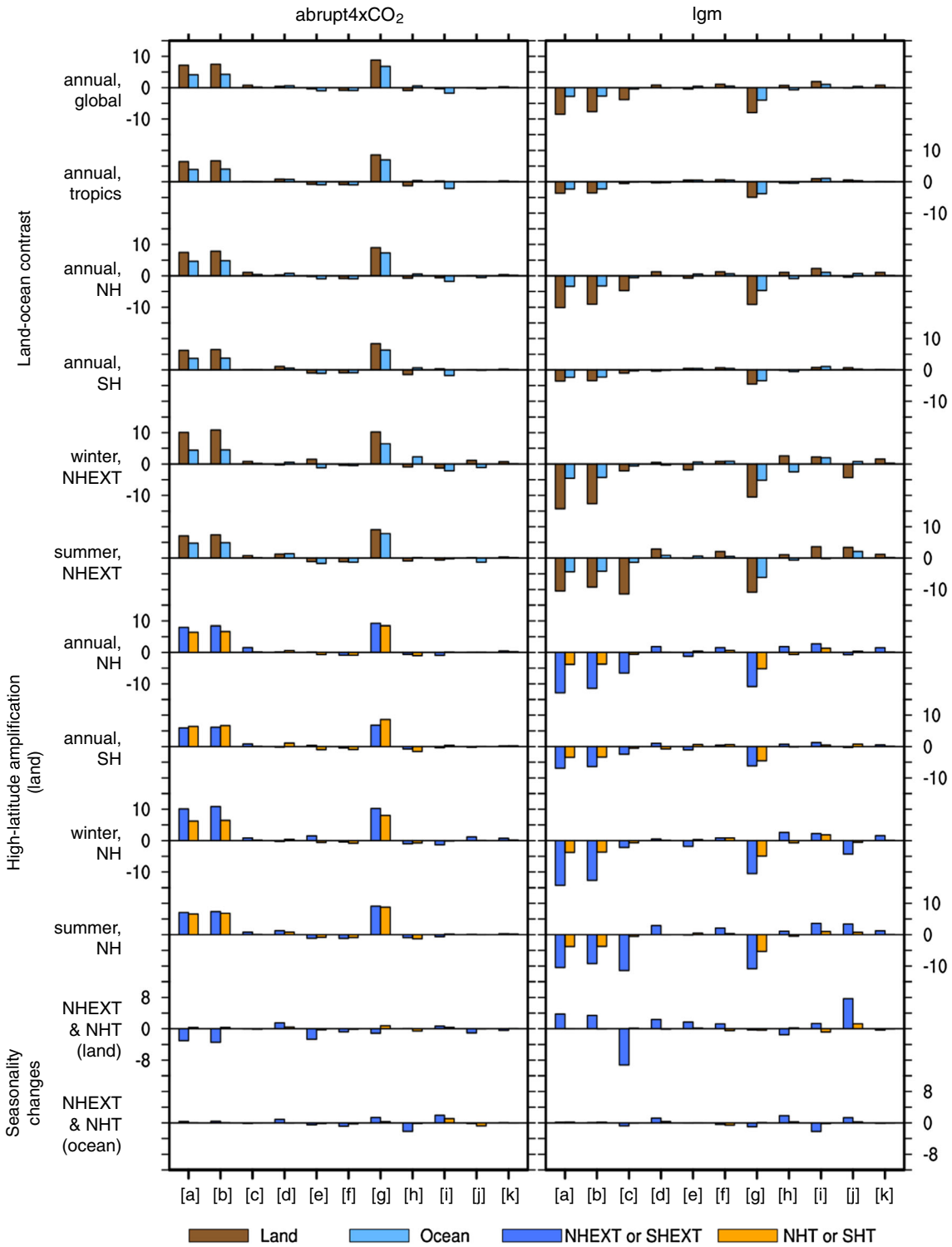

Fig. 5 Multi-model mean area-weighted averages of the anomalies in surface temperature [a] and in the partial temperature change (PTC) of each component [c through j in Eq. 11] from the energy-balance model) for the *abrupt4* × CO_2 simulation (*left*) and the *lgm* simulations (*right*) in K. Column [k] gives the change in the residual term (Eq. 12). The individual *rows* represent different aspects of the large-scale surface temperature response and its PTC: land–ocean contrast (*rows* 1–6) addressed as differences in annual temperature for the globe (60°S–85°N), tropics (30°S–30°N), northern hemisphere (NH: 0–85°N), and southern hemisphere (SH: 60°S–0), and for the northern hemisphere extratropics (NHEXT: 30–85°N) in winter (DJF mean) and summer (JJA mean); high-latitude amplification (*rows* 7–10) addressed as annual, winter and summer surface temperature differences for the Northern/Southern Hemisphere extratropics (30°N–85°N/85°S–30°S; *dark blue*) and Northern Hemisphere tropics (0–30°N/30°S–0; *orange*) respectively; seasonality (*rows* 11–12) addressed as the difference between winter and summer temperatures for the Northern Hemisphere extratropics (*dark blue*) and Northern Hemisphere tropics (*orange*) (over the land and ocean), respectively

(Figs. S4[e], S10[e]). However, $\Delta LWCRF_{surf}$ has a cooling effect over most of the world (except land-ice-covered regions such as Greenland and Antarctica) in summer conditions (Figs. S5[e], S11[e]). In the *lgm* simulations, $\Delta LWCRF_{surf}$ reduces the negative temperature anomaly over the low latitudes and the mid-latitude oceans, but reinforces negative temperature anomalies over high latitude regions (in particular, over the ice sheets and sea-ice covered areas). The changes in cloud radiative forcing (ΔCRF_{surf}) are consistent with total cloud cover changes, and the large-scale spatial patterns of $\Delta LWCRF_{surf}$ and surface shortwave cloud radiative forcing ($\Delta SWCRF_{surf}$) are opposite (AC_U is -0.76 for annual *abrupt4* $\times$ CO_2 and -0.78 annual *lgm* climate).

Downward clear-sky shortwave radiation ($(1-\overline{\alpha}_{surf})\Delta SW\downarrow_{surf}^{clr}$) always reduces the positive surface temperature anomalies (Figs. 1[f], 4[f]) in the *abrupt4* $\times$ CO_2 simulations, most markedly over the Arctic Ocean and inter-tropical convergence zone (ITCZ). The amplitude of this PTC component is larger in summer (-1.18 K) than in winter (-0.58 K). In contrast, $(1-\overline{\alpha}_{surf})\Delta SW\downarrow_{surf}^{clr}$ always increases the negative surface temperature anomalies in the *lgm* simulations, most markedly over the continental ice sheets (Figs. 2[f], 4[f]). The magnitude of the PTC over the land varies seasonally (0.67 K in summer and 1.31 K in winter). There is a very high negative correlation ($AC_U < -0.9$) between surface temperature change and $(1-\overline{\alpha}_{surf})\Delta SW\downarrow_{surf}^{clr}$ in winter, summer and annually in both climates. The spatial pattern and amplitude in both warm and cold climates is likely associated with changes in water vapor distribution, because water vapor absorbs some shortwave radiation leading to less surface warming.

The downward clear-sky longwave radiation ($\Delta LW\downarrow_{surf}^{clr}$ [g]) always reinforces the positive surface temperature anomalies in the *abrupt4* $\times$ CO_2 simulations (Figs. 1[g], 4[g]). The amplitude of the annual PTC over land (8.49 K) is larger than over the ocean (6.82 K), and the amplitude over the Arctic region is much larger than for other areas (Figs. 1[g], 4[g]). In the *lgm* simulation, this term reinforces the negative surface-temperature anomalies everywhere and in all seasons (Figs. 2, 4[g]), and again all models show the same response (Figs. S3[g], S7[g], S8[g]). As in the *abrupt4* $\times$ CO_2 simulations, the amplitude of the annual PTC over land (-8.00 K) is larger than the over ocean (-4.09 K). There is high positive correlation ($AC_U > 0.9$) between changes in surface temperature (ΔT_{surf}) and downward clear-sky longwave radiation ($\Delta LW\downarrow_{surf}^{clr}$) in all seasons in both warm and cold climates, and indeed this term displays the greatest similarly to the ΔT_{surf} of all of the energy-balance components (Figs. 1[g], 2[g], 3[g]).

In the *abrupt4* $\times$ CO_2 simulations, sensible heating ($-\Delta Q_H$[h]) reduces the positive surface temperature anomalies over most land areas (-0.89 K), and increases it over the ocean (0.57 K) except the Southern and Arctic Oceans (Figs. 1[h], 4[h]). In the *lgm* simulations, $-\Delta Q_H$ (Figs. 2[h], 4[h]) reduces the negative temperature anomaly over the continental ice sheets and some land regions (western North America, central South America, East Asia, and southern Africa). It increases the negative surface temperature anomaly over almost all ocean regions (-0.58 K), except for the Arctic and Antarctic Oceans where sensible heating reduces the negative temperature anomalies because of increased sea-ice cover. There is relatively high negative correlation ($AC_U \approx -0.6$) between surface temperature change and the PTC of this term over land throughout the year in both climates.

Latent heating ($-\Delta Q_E$[i]) reduces the positive surface-temperature anomalies over most of the globe (-1.34 K; Figs. 1[i], 4[i]) in the *abrupt4* $\times$ CO_2 simulation, except in regions where the simulated reduction in precipitation is large (e.g. northern Atlantic Ocean, southern North America, Amazon, southern Africa). The magnitude of the PTC over all grid points in winter (-1.85 K, Figs. S4[i], S10[i]) is much larger than in summer (-0.91 K, S5[i], S11[i]). In contrast, in the *lgm* simulations, $-\Delta Q_E$ results in increase in annual surface temperature (Figs. 2, 4[i]) over the most of the globe (1.35 K) and especially over the land (1.79 K). There is a relatively high negative AC_U (≈ -0.7) over the ocean between surface temperature change (ΔT_{surf}) and the latent heating ($-\Delta Q_E$) through the year in both climates.

Changes in heat storage ($-\Delta Q_G$ [j]) show much larger responses over the oceans than over the land (Figs. 1[j], 3[j], 4[j]). In the *abrupt4* $\times$ CO_2 simulations, heat storage reduces the positive surface-temperature anomaly over the Arctic Ocean in summer (Figs. S5[j], S11[j]) and increases it in winter (Figs. S4[j], S10[j]) resulting in a reduction of the positive surface temperature anomalies over the North Atlantic Ocean throughout the year. The opposite is seen in the *lgm* simulations (Figs. 2[j], 3[j], 4[j]): heat storage enhances the decrease in the surface-temperature in summer (Figs. S8[j], S11[j]) and reduces it in winter (Figs. S7[j], S10[j]) over both the Arctic and Antarctic Oceans because of changes in sea-ice cover, and helps to reduce the overall cooling in the North Atlantic. Changes in heat storage ($-\Delta Q_G$) over tropical land areas are much larger in the *lgm* simulations than the *abrupt4* $\times$ CO_2 simulations, and help to limit the surface-temperature cooling in these regions. However, globally, the impact of $-\Delta Q_G$ is small and the signs of the anomalies differ from model to model.

5 Key components of the large-scale temperature responses

We explore the key components responsible for generating land–ocean contrast, high-latitude amplification, and seasonality changes for different spatial and temporal targets for the ensemble of warm (*abrupt4* × CO_2) and cold (*lgm*) climate simulations. Figure 5 shows the amplitude of surface temperature change and PTC of each component, while Fig. 6 shows the association (spatial pattern-correlations) between CMIP5 surface temperatures and both estimated surface temperature and PTC of components. Here, we simply regard the key components of the temperature responses as those components with larger amplitudes (Fig. 5) and higher spatial correlations (Fig. 6).

5.1 Land–ocean contrast

Globally, land–ocean contrast (Fig. 5) is smaller in the annual mean *abrupt4* × CO_2 simulations (1.73) than in the annual mean *lgm* simulations (3.07), although the values for the tropics are similar (1.63 vs. 1.57). Over the Southern Hemisphere (SH, 0°–60°S), the contrast in annual mean *abrupt4* × CO_2 simulations (1.70) is larger than one in the annual mean *lgm* (1.52). The contrast over the NHEXT is larger in winter (1.80 in the *abrupt4* × CO_2 simulation, 2.99 in the *lgm*) than in summer (1.44 in *abrupt4* × CO_2, simulation, 2.32 in *lgm*). The land-sea contrast calculated using the energy-balance approach is slightly larger in the annual mean *abrupt4* × CO_2 simulations (1.77 compared to 1.73 calculated directly) but somewhat smaller in the annual mean *lgm* simulations (2.86 vs. 3.07) because of the larger positive residuals over land.

Downward clear-sky longwave radiation ($\Delta LW\downarrow_{surf}^{clr}$ [g]) is the single most important component that intensifies land–ocean contrast in the *abrupt4* × CO_2 simulations, in all regions and seasons (Figs. 5, 6). Latent heat flux ($-\Delta Q_E$ [i]) also plays an important role in intensifying land-sea contrast in annual mean climate, in particular over the tropics. Surface longwave cloud radiative forcing ($\Delta LWCRF_{surf}$ [e]) contributes to amplifying the contrast in winter and heat storage ($-\Delta Q_G$ [j]) contributes in summer over the NHEXT. Surface albedo feedback (*SAE* [c]) and downward clear-sky shortwave radiation ($(1-\overline{\alpha}_{surf})\Delta SW\downarrow_{surf}^{clr}$[f]) slightly act to amplify the contrast. Conversely, sensible heat flux ($-\Delta Q_H$ [h]) strongly reduces the contrast in all regions and seasons.

Downward clear-sky longwave radiation ($\Delta LW\downarrow_{surf}^{clr}$ [g]) is also the most important component amplifying land–ocean contrast in the *lgm* simulations (Figs. 5, 6). However, *SAE* [c] is also an important amplifier in the *lgm* simulations, except in winter over the NHEXT where change in heat storage [j] is more important in enhancing this contrast. Sensible heat flux ($-\Delta Q_H$ [h]) also contributes to reducing the contrast in winter over the NHEXT, while surface longwave cloud radiative forcing ($\Delta LWCRF_{surf}$ [e]) works to increase the contrast. Surface shortwave cloud radiative forcing ($\Delta SWCRF_{surf}$[d]), downward clear-sky shortwave radiation ($(1-\overline{\alpha}_{surf})\Delta SW\downarrow_{surf}^{clr}$[f]), sensible heat flux ($-\Delta Q_H$[h]), and latent heat flux ($-\Delta Q_E$ [i]) generally reduce land–ocean contrast in all regions and seasons.

5.2 High-latitude amplification

High-latitude amplification over the Northern Hemisphere is smaller year round in the *abrupt4* × CO_2 than in the *lgm* simulations, as would be expected given the large ice sheets in the *lgm* simulations (Fig. 5). The magnitude of the amplification is larger in winter (1.61 in *abrupt4* × CO_2, 3.77 in *lgm*) than in summer (1.08 vs. 2.78). The change estimated from the energy-balance approach ([b]) is underestimated compared to the CMIP5 multi-model mean surface temperature ([a]) in the *lgm* and overestimated in the *abrupt4* × CO_2 because of the larger residuals over the NHEXT land. On the Other hand, multi-model mean high-latitude amplification over the Southern Hemisphere does not occur under the annual mean *abrupt4* × CO_2 simulations (0.92) even though CCSM4 and MRI-CGCM3 simulate high-latitude amplification there (SI Fig. 1).

The surface albedo effect (*SAE* [c]), surface longwave cloud radiative forcing ($\Delta LWCRF_{surf}$[e]), and downward clear-sky longwave radiation ($\Delta LW\downarrow_{surf}^{clr}$ [g]) are the key components enhancing high-latitude amplification in the *abrupt4* × CO_2 simulations, although SAE does not influence amplification in winter, and $\Delta LWCRF_{surf}$ and $\Delta LW\downarrow_{surf}^{clr}$ have no impact in summer (Figs. 5, 6). On the other hand, latent heat flux ($-\Delta Q_E$ [i]) reduces the amplification especially in summer. The other energy-balance components only have a small (and inconsistent) impact on high-latitude amplification in the different seasons.

Surface albedo feedback (*SAE* [c]) and downward clear-sky longwave radiation ($\Delta LW\downarrow_{surf}^{clr}$[g]) are again the key components for enhancing high-latitude amplification under the *lgm* climate, but *SAE* [c] is more important in summer than winter; heat storage ($-\Delta Q_G$ [j]) plays a more important role in the winter amplification (Figs. 5, 6). Although surface longwave cloud radiative forcing ($\Delta LWCRF_{surf}$ [e]) and heat storage ($-\Delta Q_G$ [j]) tend to increase the amplification, surface shortwave cloud radiative forcing ($\Delta SWCRF_{surf}$ [d]), and downward clear-sky shortwave radiation ($(1-\overline{\alpha}_{surf})\Delta SW\downarrow_{surf}^{clr}$[f]), sensible

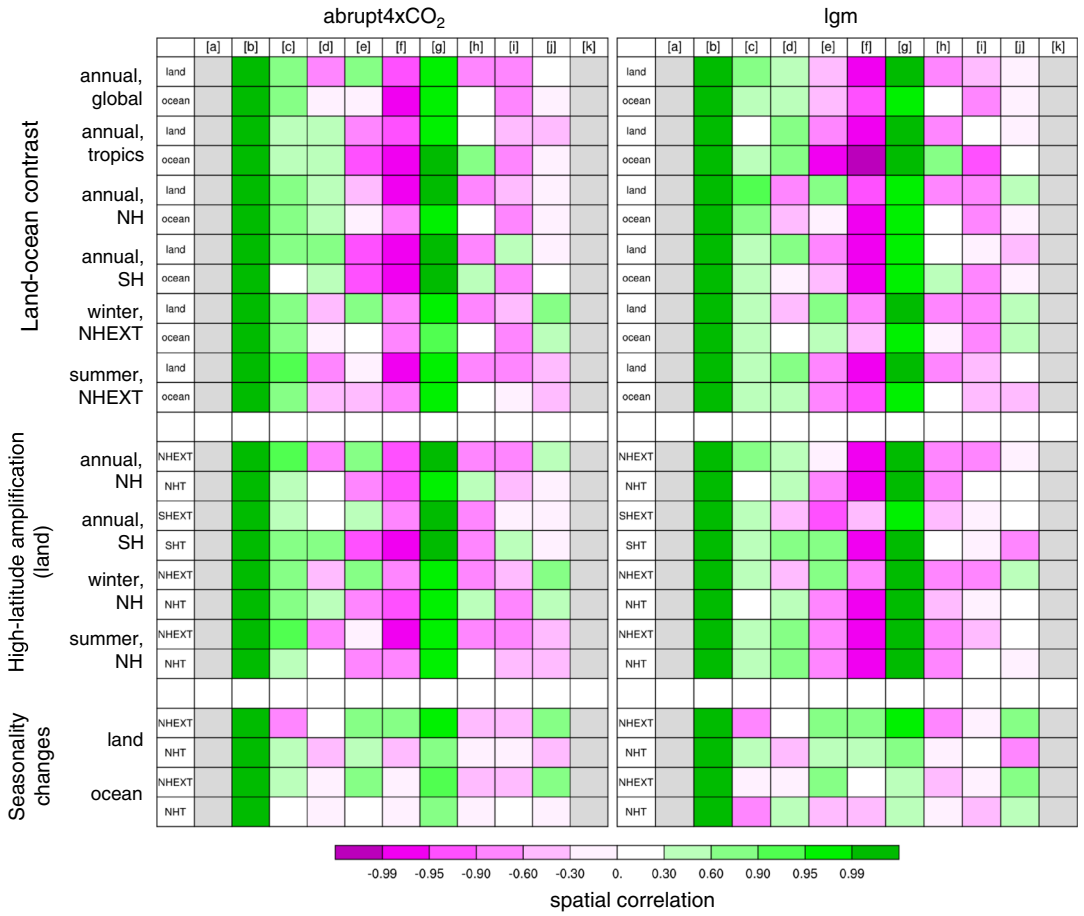

Fig. 6 Area-weighted uncentered pattern correlations between the CMIP5 surface temperature and both estimated surface temperature and its partial temperature changes (PTC) under the *abrupt4* $\times$ CO_2 simulation (*left*) and the *lgm* simulations (*right*). The individual *rows* of tables show each spatial and temporal target of large-scale surface temperature response and its PTC of each component. The *column* characters [a]–[k] correspond to the terms in the energy balance model (Eqs. 10, 11, 12). The correlation coefficient is bounded by ± 1.0; $+1.0$ indicates a perfect match between reference and simulation in spatial pattern (plotted in *green*), and -1.0 indicates the completely opposite spatial pattern (*magenta*) between reference and simulation. The correlations (and amplitude of differences) show that estimated surface temperature changes adequately reproduce the surface temperature changes and that clear-sky longwave radiation [g] is the key component of large-scale temperature changes, in particular of the land–ocean contrast and high-latitude amplification (as indicated by very high correlation coefficients and large amplitudes of changes)

heating ($-\Delta Q_H$ [h]), and latent heating ($-\Delta Q_E$ [i]) diminish the amplification.

5.3 Seasonality changes

Most of the ocean areas with regard to seasonality changes are not robust and the amplitude is quite small in both warm and cold climates (Figs. 5, S6, S9, S12). The annual cycle is reduced over high-latitude land regions and the Arctic Ocean in the *abrupt4* $\times$ CO_2 simulations (Fig. S12), but varies both longitudinally and latitudinally over middle- and low-latitude land areas (Fig. S6). No single component stands out as the dominant influence of the changes in seasonality in the *abrupt4* $\times$ CO_2 simulations: surface shortwave cloud radiative forcing ($\Delta SWCRF_{surf}$ [d]) increases seasonality and surface longwave cloud radiative forcing ($\Delta LWCRF_{surf}$ [e]) reduces seasonality in both NHT and NHEXT areas; downward clear-sky longwave radiation ($\Delta LW\downarrow^{clr}_{surf}$[g]) reduces seasonality in higher latitudes and intensifies it in low- and mid-latitudes of North America and Europe; sensible heating ($-\Delta Q_H$[h]) reduces and latent heating ($-\Delta Q_E$[i]) intensifies seasonality in the tropics.

The pattern of seasonality changes in the *lgm* simulations is spatially complex, such that the large-scale averages (NHEXT and NHT) do not provide a coherent picture (Fig. S9). Seasonality is reduced over the land-ice regions in North America, but is enhanced over the land-ice

regions in Europe (Fig. S9). However, the temperature patterns are consistent with the pattern of downward clear-sky longwave radiation ($\Delta LW\downarrow_{surf}^{clr}$[g]). The other components in the energy balance model show similar responses over the NHEXT land areas and sea-ice covered areas of the Arctic Ocean: surface albedo (*SAE* [c]) and sensible heating ($-\Delta Q_H$ [h]) reduce seasonality, but all the other components increase seasonality.

6 Discussion and conclusions

While several energy-balance components are involved in surface temperature changes, only certain components show robust and consistent patterns across multiple models in both warm and cold climates. Changes in surface downward clear-sky longwave radiation ($LW\downarrow_{surf}^{clr}$) show a very high positive spatial correlation with changes in surface temperature, robustly accounting for most of the overall change in surface temperature in both warm and cold climates. The surface albedo effect (*SAE*) makes a large contribution to surface-temperature changes in summer over the high latitudes in both warm and cold climates. In contrast, some other components, such as non-radiative fluxes and surface longwave cloud radiative forcing ($LWCRF_{surf}$), have limited influence on the large-scale temperature responses.

Our results identify surface downward clear-sky longwave radiation ($LW\downarrow_{surf}^{clr}$) as the most important component in the amplification of land–ocean contrast in both warm and cold climates in all regions and seasons. Similar results for a warm-climate state were found by Lu and Cai (2009). These results support the idea that ocean-forced changes in atmospheric circulation and water–vapor transport play a significant role in generating land–ocean contrast through temperature and humidity changes in the upper troposphere (Santer et al. 2005; Karl et al. 2006), which in turn generate changes in surface downward clear-sky longwave radiation over land (Compo and Sardeshmukh 2009). Differences in tropospheric lapse rates over land and ocean, caused by constraints on moisture availability over land compared to the ocean (see e.g. Li et al. 2013; Byrne and O'Gorman 2013b) also affect land–ocean contrast (Joshi et al. 2008; Byrne and O'Gorman 2013a): while the dry adiabatic lapse rate is independent of saturation specific humidity, the saturated adiabatic lapse rate decreases/increases with increasing/decreasing saturation specific humidity. Different changes in lapse rates over land and ocean imply different changes in surface temperature, with larger changes over the land than over the ocean. To explore in detail the relationship between our result and previous studies, $LW\downarrow_{surf}^{clr}$ must be decomposed to show the separate effects of changes in CO_2, water vapor, and direct LW feedback.

In contrast, previous studies (e.g. Sutton et al. 2007; Laine et al. 2009) have suggested that non-radiative fluxes, i.e. latent heat flux (Q_E) and sensible heat flux (Q_H), play a major role in the generation of land–ocean contrast; this is not borne out by our analyses. While Q_E apparently intensifies land–ocean contrast in the annual mean in the *abrupt4* × CO_2 simulation, this comes about through changes in seasonal heat storage (Q_G). Furthermore latent heat flux does not contribute to the intensification of land–ocean contrast in the *lgm* climate. Our analyses also indicate that neither surface shortwave cloud radiative forcing ($SWCRF_{surf}$) nor the GHG effects of downward clear-sky shortwave radiation have a strong impact on the intensification of land–ocean temperature contrast, although some previous studies have argued that both are important (e.g. Joshi and Gregory 2008; Dong et al. 2009).

Our analyses show that surface downward clear-sky longwave radiation ($LW\downarrow_{surf}^{clr}$) is also a key component for intensifying high-latitude amplification in both warm and cold climates (see also Lu and Cai (2009)). These results are consistent with previous work on high-latitude amplification in warm climates (e.g. Graversen and Wang 2009; Winton 2006) showing that changes in atmospheric water vapor lead to increased air temperature and reduced sea-ice cover and thus engender a strong longwave radiation feedback. Solomon (2006) has argued that an increase in the meridional, atmospheric energy transport in the Northern Hemisphere is to be expected in a warmer climate, because more latent heat energy release will occur over the oceans leading to increased baroclinicity. Moreover, an increase in atmospheric water vapor will increase the greenhouse effect in the Arctic more than in lower latitudes, linked in part to stable stratified conditions over the Arctic which inhibits mixing (Alexeev et al. 2005; Langen and Alexeev 2007; Lu and Cai 2010).

The surface albedo effect (*SAE*) is important in both land–ocean contrast and high-latitude amplification. We have shown that *SAE* strongly enhances land–ocean contrast in the *lgm* climate, although it is not important in the warm climate state. *SAE* enhances the *lgm* land–ocean contrast because of the presence of large continental ice sheets and extensive snow cover in the high-latitude regions. The additional contribution of *SAE* in the *lgm* experiment helps to explain the larger amplitude of land–ocean contrast in cold than warm climates (Izumi et al. 2013). The surface albedo effect also plays a significant role in generating the high-latitude amplification in summer (and hence in annual average) in both warmer and cooler climates. However, *SAE* does not contribute to high-latitude amplification in winter, which is primarily the result of changes in heat storage. Amplification of the temperature changes is not confined to strictly polar

regions (Brady et al. 2013)—pointing to the contributing role of ice- and snow-albedo feedback in generating this large-scale temperature response, particularly in winter (e.g. Screen and Simmonds 2010b).

Our results suggest that, while important, the surface albedo effect (*SAE*) is secondary to surface downward clear-sky longwave radiation ($LW\downarrow_{surf}^{clr}$) in the intensification of high-latitude amplification. This is consistent with previous studies. For example, high-latitude amplification occurred in a CCSM3 simulation in which albedo was fixed (Graversen and Wang 2009) and in an idealized GCM simulation in which ice-albedo feedback is absent (Lu and Cai 2010), and thus *SAE* could not be involved. Moreover, high-latitude amplification is found in aquaplanet simulations in which ice-albedo feedback was excluded, resulting from the impact of changes in longwave radiation and turbulent fluxes on high-latitude surface temperature (Alexeev et al. 2005; Langen and Alexeev 2007). Thus, we suggest that $LW\downarrow_{surf}^{clr}$ is the dominant factor leading to high-latitude amplification (Lu and Cai 2009), and *SAE* contributes to the intensification during summer.

The generation of changes in seasonality in response to year-round changes in forcing is a robust feature in both warm and cold climates, although the nature of the change varies between land and ocean and between high- and low-latitudes (e.g. Mann and Park 1996; Dwyer et al. 2012; Izumi et al. 2013). In contrast with the other large-scale temperature responses, no single factor stands out as the major mechanism explaining the simulated seasonality changes. In the *abrupt4* × CO_2 climate, the seasonality changes at high-latitudes are produced through changes in both surface longwave cloud radiative forcing ($LWCRF_{surf}$) and surface downward clear-sky longwave radiation ($LW\downarrow_{surf}^{clr}$). However, neither component is important in the *lgm* climate, where heat storage (Q_G) intensifies high-latitude seasonality and the surface albedo effect (*SAE*) reduces it. Although $LWCRF_{surf}$ contributes to the simulated change in seasonality in low latitudes in the *abrupt4* × CO_2 simulations, it is not important in the *lgm* simulations. Our analyses therefore suggest that simulated changes in seasonality are a consequence of the changes in land–ocean and high-latitude/low-latitude contrasts rather than an independent temperature response to the large-scale forcing.

Changes in land–ocean contrast and high-latitude amplification are robust features of climate-model simulations of the future (e.g. Joshi et al. 2013; Taylor et al. 2013; Byrne and O'Gorman 2013b) and a wide range of different palaeoclimates (e.g. Otto-Bliesner et al. 2006; Dowsett et al. 2012; Laine et al. 2009). These responses are shown by palaeoclimate data (e.g. Kageyama et al. 2013; Dowsett et al. 2012; Harrison et al. 2013; Izumi et al. 2013) and thus are features of the real climate rather than simply modeled responses. These responses can be explained through changes in the surface energy balance, but most specifically through a small number of feedbacks impacting surface downward clear-sky longwave radiation ($LW\downarrow_{surf}^{clr}$). Although several previous studies have pointed to the importance of $LW\downarrow_{surf}^{clr}$ in explaining large-scale temperature responses, they have tended to focus on single experiments and/or regions. Here, we have been able to provide a more comprehensive explanation of these large-scale phenomena through combining analyses of past and future climates. This demonstrates the way in which palaeoclimate simulations are a useful adjunct to analyses of modern-day climates in understanding the fundamental mechanisms of climate change.

Acknowledgments We acknowledge the World Climate Research Programme's Working Group on Coupled Modelling, which is responsible for CMIP, and the climate modeling groups for producing and making available their model output. (For CMIP the U.S. Department of Energy's Program for Climate Model Diagnosis and Intercomparison provides coordinating support and led development of software infrastructure in partnership with the Global Organization for Earth System Science Portals.) Thanks are also extended to E.K. Schneider (editor) and the two anonymous reviewers for their positive comments about the importance of this work, and their support for the overall structure of the paper. The analyses and figures are based on data archived by 18 June 2013. Research was supported by the U.S. National Science Foundation grant ATM-0602409.

References

Abbot DS, Walker CC, Tziperman E (2009) Can a convective cloud feedback help to eliminate winter sea ice at high CO_2 concentrations? J Clim 22(21):5719–5731. doi:10.1175/2009jcli2854.1

Alexeev VA, Langen PL, Bates JR (2005) Polar amplification of surface warming on an aquaplanet in "ghost forcing" experiments without sea ice feedbacks. Clim Dyn 24(7–8):655–666. doi:10.1007/s00382-005-0018-3

Biasutti M, Sobel AH (2009) Delayed Sahel rainfall and global seasonal cycle in a warmer climate. Geophys Res Lett 36. doi:10.1029/2009gl041303

Braconnot P, Harrison SP, Kageyama M, Bartlein PJ, Masson-Delmotte V, Abe-Ouchi A, Otto-Bliesner B, Zhao Y (2012) Evaluation of climate models using palaeoclimatic data. Nat Clim Change 2(6):417–424. doi:10.1038/nclimate1456

Brady EC, Otto-Bliesner BL, Kay JE, Rosenbloom N (2013) Sensitivity to glacial forcing in the CCSM4. J Clim 26(6):1901–1925. doi:10.1175/jcli-d-11-00416.1

Byrne MP, O'Gorman PA (2013a) Land-ocean warming contrast over a wide range of climates: convective quasi-equilibrium theory and idealized simulations. J Clim. doi:10.1175/JCLI-D-12-00262.1

Byrne MP, O'Gorman PA (2013b) Link between land–ocean warming contrast and surface relative humidities in simulations with coupled climate models. Geophys Res Lett. doi:10.1002/grl.50971

Compo GP, Sardeshmukh PD (2009) Oceanic influences on recent continental warming. Clim Dyn 32(2–3):333–342. doi:10.1007/s00382-008-0448-9

Deser C, Tomas R, Alexander M, Lawrence D (2010) The seasonal atmospheric response to projected Arctic sea ice loss in the late twenty-first century. J Clim 23(2):333–351. doi:10.1175/2009jcli3053.1

Dong B, Gregory JM, Sutton RT (2009) Understanding land-sea warming contrast in response to increasing greenhouse gases. Part I: transient adjustment. J Clim 22(11):3079–3097. doi:10.1175/2009jcli2652.1

Dowsett HJ, Robinson MM, Haywood AM, Hill DJ, Dolan AM, Stoll DK, Chan W-L, Abe-Ouchi A, Chandler MA, Rosenbloom NA, Otto-Bliesner BL, Bragg FJ, Lunt DJ, Foley KM, Riesselman CR (2012) Assessing confidence in Pliocene sea surface temperatures to evaluate predictive models. Nat Clim Change 2(5):365–371. http://www.nature.com/nclimate/journal/v2/n5/abs/nclimate1455.html-supplementary-information

Dwyer J, Biasutti B, Sobel A (2012) Projected changes in the seasonal cycle of surface temperature. J Clim. doi:10.1175/JCLI-D-11-00741.1

Fasullo JT (2010) Robust land-ocean contrasts in energy and water cycle feedbacks. J Clim 23(17):4677–4693. doi:10.1175/2010jcli3451.1

Gleckler PJ, Taylor KE, Doutriaux C (2008) Performance metrics for climate models. J Geophys Res Atmos 113(D6). doi:10.1029/2007jd008972

Graversen RG, Wang M (2009) Polar amplification in a coupled climate model with locked albedo. Clim Dyn 33(5):629–643. doi:10.1007/s00382-009-0535-6

Graversen RG, Mauritsen T, Tjernstrom M, Kallen E, Svensson G (2008) Vertical structure of recent Arctic warming. Nature 451(7174):U53–U54. doi:10.1038/nature06502

Hall A (2004) The role of surface albedo feedback in climate. J Clim 17(7):1550–1568. doi:10.1175/1520-0442(2004)017<1550:trosaf>2.0.co;2

Harrison SP, Bartlein PJ, Brewer S, Prentice IC, Boyd M, Hessler I, Holmgren K, Izumi K, Willis K (2013) Climate model benchmarking with glacial and mid-Holocene climates. Clim Dyn 1–18. doi:10.1007/s00382-013-1922-6

Holland MM, Bitz CM (2003) Polar amplification of climate change in coupled models. Clim Dyn 21(3–4):221–232. doi:10.1007/s00382-003-0332-6

Holland MM, Bitz CM, Tremblay B, Bailey DA (2008) The role of natural versus forced change in future rapid summer Arctic ice loss. In: DeWeaver ET, Bitz CM, Tremblay L-B (eds) Arctic sea ice decline: observations, projections, mechanisms, and implications. American Geophysical Union, Washington, DC

Izumi K, Bartlein PJ, Harrison SP (2013) Consistent large-scale temperature responses in warm and cold climates. Geophys Res Lett 40(9):1817–1823. doi:10.1002/grl.50350

Jackson JM, Carmack EC, McLaughlin FA, Allen SE, Ingram RG (2010) Identification, characterization, and change of the near-surface temperature maximum in the Canada Basin, 1993–2008. J Geophys Res Oceans 115. doi:10.1029/2009jc005265

Jin M, Liang S (2006) An improved land surface emissivity parameter for land surface models using global remote sensing observations. J Clim 19(12):2867–2881. doi:10.1175/jcli3720.1

Joshi M, Gregory J (2008) Dependence of the land-sea contrast in surface climate response on the nature of the forcing. Geophys Res Lett 35(24). doi:10.1029/2008gl036234

Joshi MM, Gregory JM, Webb MJ, Sexton DMH, Johns TC (2008) Mechanisms for the land/sea warming contrast exhibited by simulations of climate change. Clim Dyn 30(5):455–465. doi:10.1007/s00382-007-0306-1

Joshi MM, Lambert FH, Webb MJ (2013) An explanation for the difference between twentieth and twenty-first century land–sea warming ratio in climate models. Clim Dyn 41(7–8):1853–1869. doi:10.1007/s00382-013-1664-5

Kageyama M, Braconnot P, Bopp L, Mariotti V, Roy T, Woillez M-N, Caubel A, Foujols M-A, Guilyardi E, Khodri M, Lloyd J, Lombard F, Marti O (2013) Mid-Holocene and last glacial maximum climate simulations with the IPSL model: part II: model-data comparisons. Clim Dyn 40(9–10):2469–2495. doi:10.1007/s00382-012-1499-5

Karl TR, Hassol SJ, Miller CD, Murray WL (2006) Temperature trends in the lower atmosphere: steps for understanding and reconciling differences. Synthesis and Assessment Product 1.1. U.S. Climate Change Science Program, Washington, DC

Laine A, Kageyama M, Braconnot P, Alkama R (2009) Impact of greenhouse gas concentration changes on surface energetics in IPSL-CM4: regional warming patterns, land-sea warming ratios, and glacial-interglacial differences. J Clim 22(17):4621–4635. doi:10.1175/2009jcli2771.1

Langen PL, Alexeev VA (2007) Polar amplification as a preferred response in an idealized aquaplanet GCM. Clim Dyn 29(2–3):305–317. doi:10.1007/s00382-006-0221-x

Leibowicz BD, Abbot DS, Emanuel K, Tziperman E (2012) Correlation between present-day model simulation of Arctic cloud radiative forcing and sea ice consistent with positive winter convective cloud feedback. J Adv Model Earth Syst 4. doi:10.1029/2012ms000153

Li G, Harrison SP, Bartlein PJ, Izumi K, Colin Prentice I (2013) Precipitation scaling with temperature in warm and cold climates: an analysis of CMIP5 simulations. Geophys Res Lett 40(15):4018–4024. doi:10.1002/grl.50730

Lu J, Cai M (2009) Seasonality of polar surface warming amplification in climate simulations. Geophys Res Lett 36. doi:10.1029/2009gl040133

Lu J, Cai M (2010) Quantifying contributions to polar warming amplification in an idealized coupled general circulation model. Clim Dyn 34(5):669–687. doi:10.1007/s00382-009-0673-x

Manabe S, Stouffer RJ (1980) Sensitivity of a global climate model to an increase of CO_2 concentration in the atmosphere. J Geophys Res Oceans Atmos 85(NC10):5529–5554. doi:10.1029/JC085iC10p05529

Manabe S, Stouffer RJ, Spelman MJ, Bryan K (1991) Transient responses of a coupled ocean atmosphere model to gradual changes of atmospheric CO_2. I. Annual mean response. J Clim 4(8):785–818. doi:10.1175/1520-0442(1991)004<0785:troaco>2.0.co;2

Mann ME, Park J (1996) Greenhouse warming and changes in the seasonal cycle of temperature: model versus observations. Geophys Res Lett 23(10):1111–1114. doi:10.1029/96gl01066

Masson-Delmotte V, Kageyama M, Braconnot P, Charbit S, Krinner G, Ritz C, Guilyardi E, Jouzel J, Abe-Ouchi A, Crucifix M, Gladstone RM, Hewitt CD, Kitoh A, LeGrande AN, Marti O, Merkel U, Motoi T, Ohgaito R, Otto-Bliesner B, Peltier WR, Ross I, Valdes PJ, Vettoretti G, Weber SL, Wolk F, Yu Y (2006) Past and future polar amplification of climate change: climate model intercomparisons and ice-core constraints. Clim Dyn 26(5):513–529. doi:10.1007/s00382-005-0081-9

Oke TR (1987) Boundary layer climates, 2nd edn. Routledge, London

Otto-Bliesner BL, Marsha SJ, Overpeck JT, Miller GH, Hu AX, Mem CLIP (2006) Simulating arctic climate warmth and icefield retreat in the last interglaciation. Science 311(5768):1751–1753. doi:10.1126/science.1120808

Pithan F, Mauritsen T (2014) Arctic amplification dominated by temperature feedbacks in contemporary climate models. Nat Geosci 7(3):181–184. doi:10.1038/ngeo2071

Santer BD, Wigley TML, Mears C, Wentz FJ, Klein SA, Seidel DJ, Taylor KE, Thorne PW, Wehner MF, Gleckler PJ, Boyle JS, Collins WD, Dixon KW, Doutriaux C, Free M, Fu Q, Hansen JE, Jones GS, Ruedy R, Karl TR, Lanzante JR, Meehl GA, Ramaswamy V, Russell G, Schmidt GA (2005) Amplification of surface temperature trends and variability in the tropical atmosphere. Science 309(5740):1551–1556. doi:10.1126/science.1114867

Santer BD, Mears C, Wentz FJ, Taylor KE, Gleckler PJ, Wigley TML, Barnett TP, Boyle JS, Brueggemann W, Gillett NP, Klein SA, Meehl GA, Nozawa T, Pierce DW, Stott PA, Washington WM, Wehner MF (2007) Identification of human-induced changes in atmospheric moisture content. Proc Natl Acad Sci USA 104(39):15248–15253. doi:10.1073/pnas.0702872104

Screen JA, Simmonds I (2010a) The central role of diminishing sea ice in recent Arctic temperature amplification. Nature 464(7293):1334–1337. doi:10.1038/nature09051

Screen JA, Simmonds I (2010b) Increasing fall-winter energy loss from the Arctic Ocean and its role in Arctic temperature amplification. Geophys Res Lett 37. doi:10.1029/2010gl044136

Serreze MC, Barry RG (2011) Processes and impacts of Arctic amplification: a research synthesis. Glob Planet Change 77(1–2):85–96. doi:10.1016/j.gloplacha.2011.03.004

Serreze MC, Barrett AP, Stroeve JC, Kindig DN, Holland MM (2009) The emergence of surface-based Arctic amplification. Cryosphere 3(1):11–19

Shupe MD, Intrieri JM (2004) Cloud radiative forcing of the Arctic surface: the influence of cloud properties, surface albedo, and solar zenith angle. J Clim 17(3):616–628. doi:10.1175/1520-0442(2004)017<0616:crfota>2.0.co;2

Sobel AH, Bretherton CS (2000) Modeling tropical precipitation in a single column. J Clim 13(24):4378–4392. doi:10.1175/1520-0442(2000)013<4378:mtpias>2.0.co;2

Sobel AH, Camargo SJ (2011) Projected future seasonal changes in tropical summer climate. J Clim 24(2):473–487. doi:10.1175/2010jcli3748.1

Soden BJ, Broccoli AJ, Hemler RS (2004) On the use of cloud forcing to estimate cloud feedback. J Clim 17(19):3661–3665. doi:10.1175/1520-0442(2004)017<3661:otuocf>2.0.co;2

Solomon A (2006) Impact of latent heat release on polar climate. Geophys Res Lett 33(7). doi:10.1029/2005gl025607

Stine AR, Huybers P (2012) Changes in the seasonal cycle of temperature and atmospheric circulation. J Clim 25(21):7362–7380. doi:10.1175/jcli-d-11-00470.1

Stine AR, Huybers P, Fung IY (2009) Changes in the phase of the annual cycle of surface temperature. Nature 457(7228):U431–U435. doi:10.1038/nature07675

Sutton RT, Dong B, Gregory JM (2007) Land/sea warming ratio in response to climate change: IPCC AR4 model results and comparison with observations. Geophys Res Lett 34(2). doi:10.1029/2006gl028164

Taylor KE, Stouffer RJ, Meehl GA (2012) An overview of CMIP5 and the experiment design. Bull Am Meteorol Soc 93(4):485–498. doi:10.1175/bams-d-11-00094.1

Taylor PC, Cai M, Hu A, Meehl J, Washington W, Zhang GJ (2013) A decomposition of feedback contributions to polar warming amplification. J Clim 26(18):7023–7043. doi:10.1175/jcli-d-12-00696.1

Thomson DJ (1995) The seasons, global temperature, and precession. Science 268(5207):59–68. doi:10.1126/science.268.5207.59

Wallace CJ, Osborn TJ (2002) Recent and future modulation of the annual cycle. Clim Res 22(1):1–11. doi:10.3354/cr022001

Wilks DS (2011) Statistical methods in the atmospheric sciences, 3rd edn. International geophysics series, vol 100. Academic Press, New York

Winton M (2006) Amplified Arctic climate change: What does surface albedo feedback have to do with it? Geophys Res Lett 33(3). doi:10.1029/2005gl025244